

Supplementary information for Facile integration of electro-optic SiO₂/ITO heteroin- terfaces in MIS structures for CMOS-compatible plas- monic waveguide modulation

*Nasir Alfaraj Charles Chih-Chin Lin Sherif Nasif Swati Rajput Amr S. Helmy**

The Edward S. Rogers Sr. Department of Electrical and Computer Engineering, University of Toronto,
Ontario M5S 3G4, Canada

Email Address: a.helmy@utoronto.ca

1 ITO epsilon-near-zero properties

In general, the response of a metal to an external E-field is defined by electron gas plasma oscillations, which influences the permittivity of the metal in accordance with the Thomas–Fermi screening microscopic model [1, 2, 3]. Following this approach, the complex permittivity of a metal $\varepsilon(\omega)$ can be expressed as a function of light frequency ω using the Drude model of electrical conduction, [4, 5, 3]

$$\varepsilon(\omega) = 1 - \frac{\omega_p^2}{\omega^2(1 + j\frac{1}{\omega\tau})}, \quad (1)$$

where

$$\omega_p = \sqrt{q^2 n / (\varepsilon_0 m^*)} \quad (2)$$

is the plasma frequency of the metal (i.e., the resonant frequency of free electron gas in the metal), n is the density of electrons in the metal, ε_0 is the vacuum permittivity, m^* is the effective electron mass, $q \approx 1.602 \times 10^{-19}$ C is the elementary charge, and τ is the electron relaxation time in that metal, which, along with the frequency dependence of the metal's conductivity, determines the Drude response of the metal. When $\omega\tau \gg 1$, one can neglect electron collisions in the metal's crystal lattice, and equation (1) reduces to the following approximation

$$\varepsilon(\omega) = 1 - \frac{\omega_p^2}{\omega^2}, \quad \text{for } \omega\tau \gg 1. \quad (3)$$

From equation (3), we can deduce the following:

$$\omega_p \gg \omega \Rightarrow \varepsilon(\omega) \rightarrow -\infty, \quad (4)$$

$$\omega_p \approx \omega \Rightarrow \varepsilon(\omega) \rightarrow 0, \quad (5)$$

$$\omega_p \ll \omega \Rightarrow \varepsilon(\omega) \rightarrow 1. \quad (6)$$

Equation (4) implies that the permittivity is negative when the light frequency ω is lower than the plasma frequency of the metal ω_p . Equation (5) describes the ENZ mode; the permittivity $\varepsilon(\omega)$, of the metal layer converges to zero as the plasma frequency becomes closer in value to the light frequency. ENZ metamaterials and plasmonic materials pertain to a material category whose constituent metastructures have profoundly subwavelength thicknesses in which $\varepsilon(\omega)$ approaches values close to zero for a given incident light frequency [6]. More specifically, when that frequency is near the plasma frequency ω_p of a transparent conducting oxide (TCO), e.g. ITO, the real part of $\varepsilon(\omega)$ attains a near-zero value. On the other hand, the imaginary part of $\varepsilon(\omega)$ is negligible [7]. The ENZ mode makes up a portion of the long-range surface plasmon mode, and therefore is a transverse electric (TE) mode [8]. Moreover, for conductive media with thicknesses significantly smaller than the skin depth δ , the plasma resonance can be easily seen and an approximation using a linear relation between ω and the transverse component of

the wave vector can be employed. The ENZ-related E-field across a film increases in magnitude when its thickness decreases. When exploited right, this phenomenon can create a multitude of new applications, such as more efficient electro-optical modulation [9]. For ITO with free carrier density $n \approx 6.3 \times 10^{20} \text{ cm}^{-3}$, the ENZ regime lies at a light wavelength λ of 1550 nm, corresponding to $\hbar\omega = 790 \text{ meV}$ as discerned from Figure S1(b). The dielectric constant of ITO as a function of depth z into the ITO layer, $\varepsilon_{\text{ITO}}(z)$, can be determined using

$$\varepsilon_{\text{ITO}}(z) = \varepsilon_{\infty} - \frac{q^2 N(z)}{[(\varepsilon_0 m^*)(\omega^2 + j\gamma\omega)]}, \quad (7)$$

where $\varepsilon_{\infty} = 3.9$ is the high-frequency dielectric constant of ITO, $N(z)$ is the depth-specific free carrier concentration, and $\gamma = 1.8 \times 10^{14} \text{ rad s}^{-1}$ the electron scattering rate (i.e., the inverse momentum relaxation time or collision frequency). At a specific depth z , the permittivity of ITO $\varepsilon_{\text{ITO}}(z, \omega)$ can be written as [10]

$$\varepsilon_{\text{ITO}}(z, \omega) = \varepsilon_{\infty} - \frac{\omega_p^2(z)}{\omega^2 - j\gamma\omega}, \quad (8)$$

where the ITO plasma frequency ω_p depends on the electron concentration n at that specific depth, which can be calculated as described following equation (1). The real part in equation (8) accounts for polarization while the imaginary part accounts for losses. Figure S1(a) plots the real and imaginary components, as well as the magnitude, of ITO permittivity as functions of accumulation layer carrier density n_{acc} at $\lambda = 1550 \text{ nm}$ using the Drude model (equation (8)), where

$$\text{Re}(\varepsilon_{\text{ITO}}(n_{\text{acc}})) = \varepsilon_{\infty} - \frac{\omega_p^2(n_{\text{acc}})}{\omega^2 + \gamma^2}, \quad (9)$$

$$\text{Im}(\varepsilon_{\text{ITO}}(n_{\text{acc}})) = -\frac{\omega_p^2(n_{\text{acc}})}{\omega(\omega^2 + \gamma^2)}\gamma, \quad (10)$$

$$|\varepsilon_{\text{ITO}}|(n_{\text{acc}}) = \sqrt{\text{Re}(\varepsilon_{\text{ITO}}(n_{\text{acc}}))^2 + \text{Im}(\varepsilon_{\text{ITO}}(n_{\text{acc}}))^2}. \quad (11)$$

Figure S1(b) plots $\text{Re}(\varepsilon_{\text{ITO}})$, $\text{Im}(\varepsilon_{\text{ITO}})$, and $|\varepsilon_{\text{ITO}}|$ as functions of radial light frequency (i.e., light photon energy $\hbar\omega$). To calculate ω_p of ITO, we presumed $n_{\text{acc}} = 6.3 \times 10^{20} \text{ cm}^{-3}$ and $m^*/m_0 = 0.35$. The former corresponds to a carrier density value within the ENZ regime as determined using equation (1) and shown in Figure S1(a). As one can see in Figure S1(b), as the light wavelength increases, the sign of $\text{Re}(\varepsilon_{\text{ITO}})$ changes from negative to positive at approximately $\hbar\omega = 790 \text{ meV}$ (or $\lambda = 1550 \text{ nm}$). When $|\varepsilon_{\text{ITO}}|$ is in the ENZ regime, that is, $-1 < |\varepsilon_{\text{ITO}}| < 1$, a large E-field enhancement occurs in the accumulation layer for NIR wavelengths, allowing for an efficient electrical modulation of the attributes of nanoscale optoelectronic devices (i.e., high-speed modulation with low power consumption) [11, 12, 13, 14, 10].

When the operating frequency of an ITO-based device is near the plasma frequency of ITO, the real and imaginary parts of ITO permittivity are strongly suppressed [15]. In a hybrid plasmonic waveguide, the absorbed areal power and field intensity are proportional to the dielectric spacer's $\text{Im}(\varepsilon_r)/|\varepsilon_r|$ ratio. Therefore, as $|\varepsilon_r| \rightarrow 0$, it is possible to absorb EM energy from the high-index Si core and the dielectric spacer layers and localize the optical field within the accumulation region of ITO. Because of the strong free carrier absorption and ohmic losses originating from the neighboring metal layer, the mode propagation length is significantly reduced. As a result, under the assumption of uniform carrier accumulation, the ENZ effects enable refractive index change within a 1 nm-thick accumulation layer to significantly disturb a well-guided hybrid plasmonic mode [16, 14].

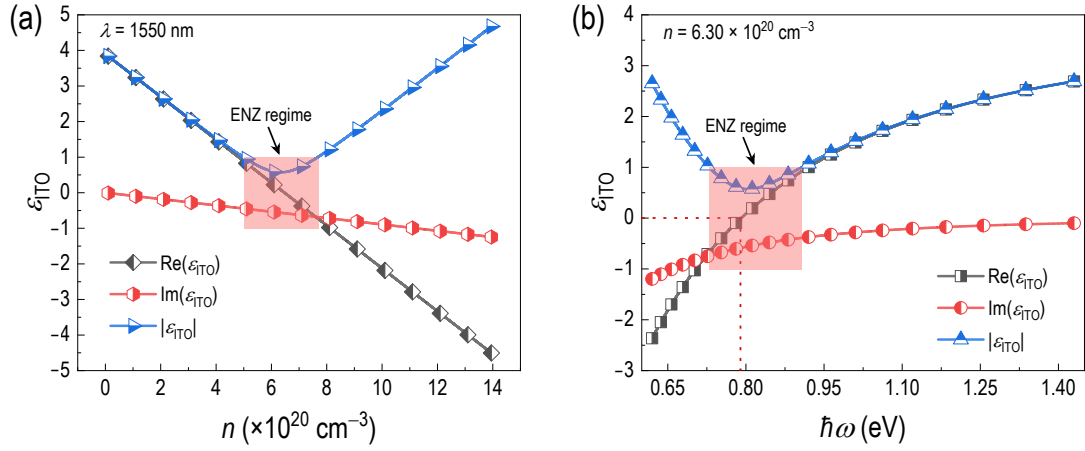


Figure S1: ITO optical attributes—(a) Plot of the real and imaginary components, as well as the magnitude, of ITO permittivity as a function of accumulation layer carrier density at $\lambda = 1550 \text{ nm}$ using Drude model (equation (8)). (b) Plot of ITO permittivity as a function of light energy using the simplified Drude model (equations (3)). The shaded regions indicate the ENZ regime.

2 Atomic force microscopy analysis

Figure S2 shows AFM images of deposited TiN and SiO_2 surfaces thin films. The root mean square (RMS) roughnesses of the TiN and SiO_2 layers are 1.12 nm and 1.36 nm, respectively.

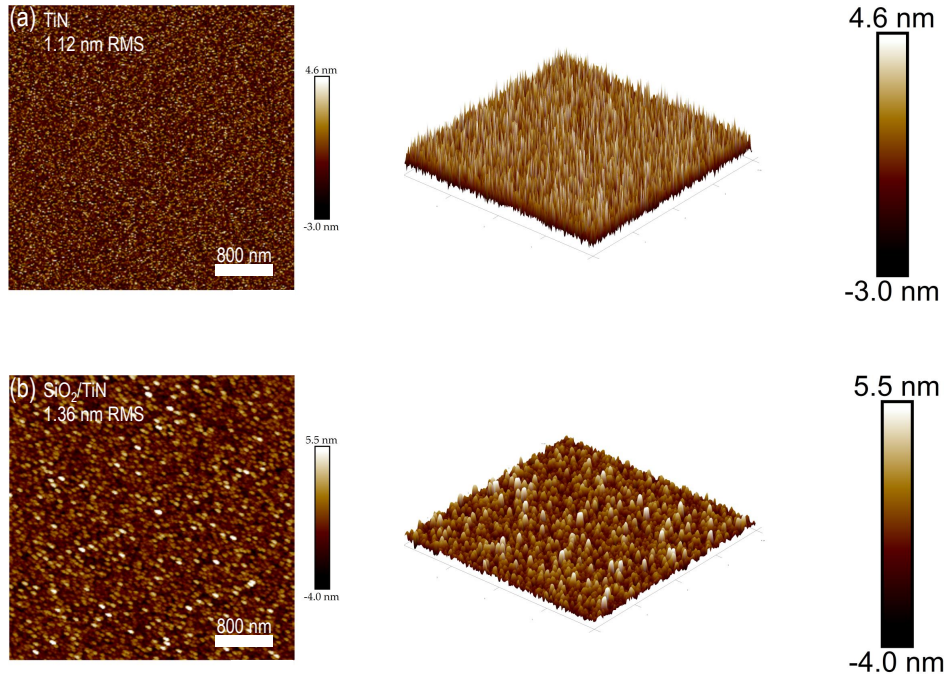


Figure S2: AFM map images of the deposited (a) TiN and (b) SiO_2 surfaces.

3 Charge transport solver

Taking advantage of its self-consistent algorithm, a charge solver, namely Lumerical DEVICE (CHARGE module), was used to plot the theoretical carrier density concentration and estimate the accumulation layer thickness. By solving the drift-diffusion equation for electrons and holes

$$\mathbf{J}_n = q\mu_n n \mathbf{E} + qD_n \nabla n, \quad (12)$$

$$\mathbf{J}_p = q\mu_p p \mathbf{E} + qD_p \nabla p, \quad (13)$$

where \mathbf{J}_n and \mathbf{J}_p are the current density vectors resulting from electron and hole transportation, respectively, μ_n and μ_p are the carrier mobilities, \mathbf{E} is the E-field vector, and D_n and D_p are the carrier diffusion coefficients, and n and p are the carrier densities. Evidently from equation (12) and (13), each charge carrier undergoes several transport processes under the effect of two competing mechanisms, namely carrier drift and diffusion. The former is caused by the applied E-field, whereas the latter is induced by the gradient in carrier density. The carrier diffusion coefficients are determined using the Einstein relation,

$$D_{n,p} = \mu_{n,p} \frac{k_B T}{q}, \quad (14)$$

where k_B is the Boltzmann constant. To solve the drift-diffusion equations, the applied E-field must be determined. To obtain the E-field, Poisson's equation

$$-\nabla \cdot (\varepsilon \nabla V) = q\rho, \quad (15)$$

must be solved, where ε is the dielectric constant, V the electrostatic potential ($\mathbf{E} = -\nabla V$), and ρ the net charge density. To account for charge conservation, the continuity equations that describe charge carrier transport are solved

$$\frac{\partial n}{\partial t} = \frac{1}{q} \nabla \cdot \mathbf{J}_n - R_n, \quad (16)$$

$$\frac{\partial p}{\partial t} = -\frac{1}{q} \nabla \cdot \mathbf{J}_p - R_p, \quad (17)$$

where $R_{n,p}$ is the net recombination rate. By discretizing the equations along a finite-element mesh and imposing the following condition in equations (16) and (17)

$$\frac{\partial n}{\partial t} = \frac{\partial p}{\partial t} = 0. \quad (18)$$

CHARGE can solve the drift-diffusion and Poisson's equations, resulting in steady-state solutions to the carrier density and electrostatic potential.

4 Graded-index layer model

For a metal-insulator-metal (MIM) modulator waveguide employing ITO layers in its slot region, the UAL model has traditionally been used to analyze the electrical behavior. In such a model, the ITO layer is conceptualized as a stack of two layers: a layer with an invariable permittivity and a layer with an effective permittivity tunable by virtue of a variable applied voltage. The latter layer is referred to as an accumulation layer. Put differently, in the UAL model, ITO is modeled as a homogeneous layer with an initial uniform carrier concentration N_0 and an accumulation layer with uniform carrier concentration N_a tuned electrostatically. The analysis based on this model are rendered incorrect if the applied voltage is sufficiently large; in particular, when the voltage is around the value for which the real part of the accumulation layer permittivity converges to zero and uncertainty in determining the accumulation layer thickness is warranted. Therefore, precise calculation of the carrier concentration in an ITO layer must involve a GIL model structure in which the ITO layer is perceived as a layer with a continuous and variable dielectric constant distribution [17]. Recall the Thomas-Fermi model, the carrier density N as a function of depth into the ITO layer (z) can be expressed as [18]

$$N(z) = N_0 \left(\frac{q\phi(z)}{E_F} \right)^{\frac{3}{2}}, \quad (19)$$

where $\phi(z)$ is the electric potential on which $N(z)$ is dependent and E_F is the Fermi level:

$$E_F = h^2 \frac{(3\pi^2 N_0)^{\frac{2}{3}}}{8\pi^2 m^*}, \quad (20)$$

where h is Planck's constant, $m^* = 0.35m_0$ is the effective electron mass in ITO, and $m_0 \approx 9.109 \times 10^{-31}$ kg is the rest mass of an electron. To determine $\phi(z)$, the following second-order differential equation deduced from equation (19) and Poisson's equation must be solved:

$$\frac{d^2\phi}{dz^2} = \frac{qN_0 \left[\left(q \frac{\phi(z)}{E_F} \right)^{\frac{3}{2}} - 1 \right]}{\varepsilon_{\text{ITO}} \varepsilon_0}, \quad (21)$$

with the boundary conditions

$$\left. \frac{d\phi}{dz} \right|_{z=t_{\text{ITO}}} = \left(\frac{\varepsilon_{\text{oxide}}}{\varepsilon_{\text{ITO}}} \right) \left(\frac{U}{t_{\text{oxide}}} \right), \quad (22)$$

$$\phi(-\infty) = 0. \quad (23)$$

Here, $\varepsilon_{\text{ITO}} = 9.3$ and $\varepsilon_{\text{oxide}}$ are the static dielectric constants of ITO (at low-frequencies or constant E-field) and the capping oxide layers, respectively. For HfO_2 , $\varepsilon_{\text{oxide}} = 25$, whereas for SiO_2 , $\varepsilon_{\text{oxide}} = 12$.

5 MISM device CV measurements at lower small-signal frequencies

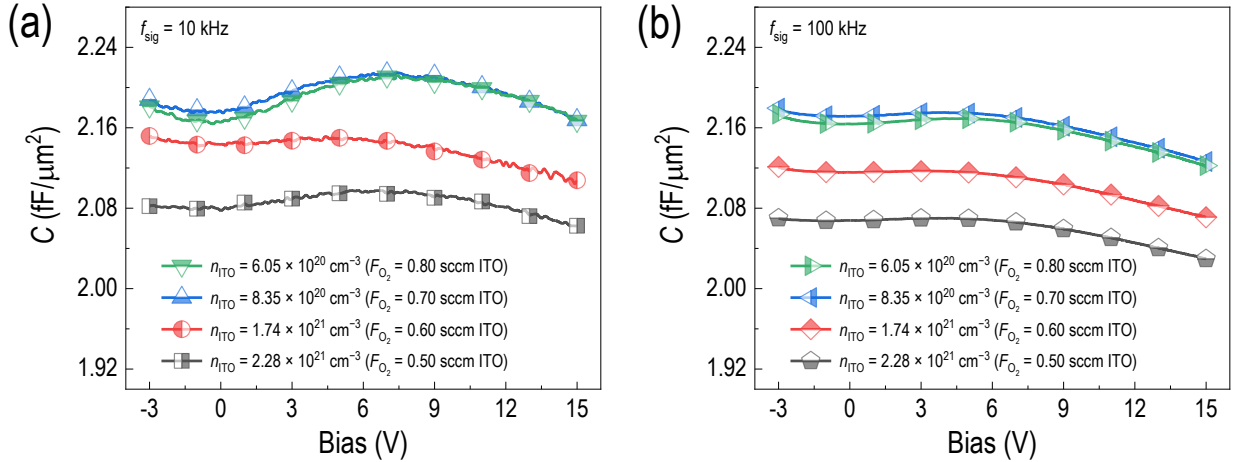


Figure S3: Frequency response curves of fabricated SiO_2/ITO MISMs with different n_{ITO} levels as functions of bias voltage at (a) 10 kHz and (b) 100 kHz.

6 MISM device CV-IV adherence curves

Figure S4 shows θ_z adherence measurements, demonstrating near-ideal MISM devices as capacitors (i.e., θ_z is as close as possible to -90°). For an ideal capacitive device, it is necessary that θ_z (i.e., the angle between I and V) be -90° , implying that there is no external influence of R_s on measured Z and therefore the measured Z values are entirely imaginary ($R_s = 0 \rightarrow Z = 1/(j\omega C)$).

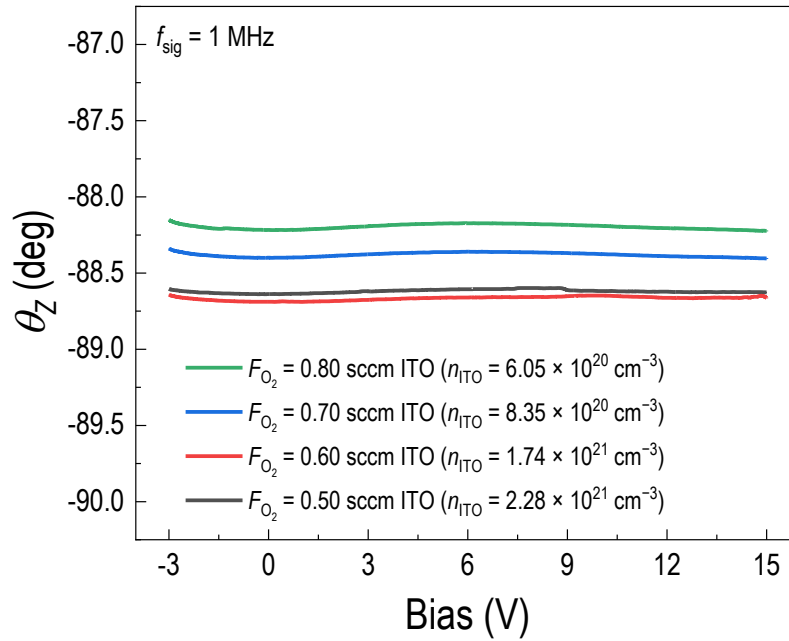


Figure S4: θ_z adherence characteristics of measured ITO-based MISM devices with different F_{O_2} at $f_{\text{sig}} = 100$ MHz.

References

- [1] A. Schlaich, D. Jin, L. Bocquet, B. Coasne, *Nat. Mater.* **2022**, *21*, 2 237.
- [2] J. Comtet, A. Niguès, V. Kaiser, B. Coasne, L. Bocquet, A. Siria, *Nat. Mater.* **2017**, *16*, 6 634.
- [3] N. W. Ashcroft, N. D. Mermin, *Solid State Physics*, Holt, Rinehart and Winston, **1976**.
- [4] J. M. Pitarke, V. M. Silkin, E. V. Chulkov, P. M. Echenique, *Rep. Prog. Phys.* **2006**, *70*, 1 1.
- [5] M. Van Exter, D. Grischkowsky, *Phys. Rev. B* **1990**, *41*, 17 12140.
- [6] M. Silveirinha, N. Engheta, *Phys. Rev. Lett.* **2006**, *97*, 15 157403.
- [7] A. Boltasseva, H. A. Atwater, *Science* **2011**, *331*, 6015 290.
- [8] Y. Li, I. Liberal, N. Engheta, *Sci. Adv.* **2019**, *5*, 10 eaav3764.
- [9] Z. Ma, Z. Li, K. Liu, C. Ye, V. J. Sorger, *Nanophotonics* **2015**, *4*, 2 198.
- [10] A. P. Vasudev, J.-H. Kang, J. Park, X. Liu, M. L. Brongersma, *Opt. Express* **2013**, *21*, 22 26387.
- [11] Y.-W. Huang, H. W. H. Lee, R. Sokhoyan, R. A. Pala, K. Thyagarajan, S. Han, D. P. Tsai, H. A. Atwater, *Nano Lett.* **2016**, *16*, 9 5319.
- [12] J. Park, J.-H. Kang, X. Liu, M. L. Brongersma, *Sci. Rep.* **2015**, *5* 15754.
- [13] H. W. Lee, G. Papadakis, S. P. Burgos, K. Chander, A. Kriesch, R. Pala, U. Peschel, H. A. Atwater, *Nano Lett.* **2014**, *14*, 11 6463.
- [14] Z. Lu, W. Zhao, K. Shi, *IEEE Photonics J.* **2012**, *4*, 3 735.
- [15] J. H. Ni, W. L. Sarney, A. C. Leff, J. P. Cahill, W. Zhou, *Sci. Rep.* **2020**, *10* 713.
- [16] C. Lin, A. S. Helmy, *Sci. Rep.* **2015**, *5* 12313.
- [17] M.-S. Kwon, *IEEE Photonics J.* **2015**, *8*, 1 4900108.
- [18] A. Melikyan, N. Lindenmann, S. Walheim, P. Leufke, S. Ulrich, J. Ye, P. Vincze, H. Hahn, T. Schimmel, C. Koos, W. Freude, J. Leuthold, *Opt. Express* **2011**, *19*, 9 8855.